Low-Cost Multi-Band Compact Branch-Line Coupler Design Using Response Features and Automated EM Model Fidelity Adjustment

Slawomir Koziel[1,2] and Adrian Bekasiewicz[1,2]

[1] Engineering Optimization & Modeling Center, School of Science and Engineering, Reykjavik University, Reykjavik, Iceland, bekasiewicz@ru.is, koziel@ru.is

[2] Faculty of Electronics Telecommunications and Informatics, Gdansk University of Technology, Gdansk, Poland

Abstract: Design closure of compact microwave components is a challenging problem because of significant electromagnetic (EM) cross-couplings in densely arranged layouts. A separate issue is a large number of designable parameters resulting from replacement of conventional transmission line sections by compact microstrip resonant cells. This increases complexity of the design optimization problem and requires employment of expensive high-fidelity EM analysis for reliable performance evaluation of the structure at hand. Consequently, neither conventional numerical optimization algorithms nor interactive approaches (e.g., experience-driven parameters sweeps) are capable of identifying optimum designs in reasonable timeframes. Here, we discuss application of feature-based optimization for fast design optimization of dual- and multi-band compact couplers. On one hand, design of such components is difficult because of multiple objectives (achieving equal power split as well as good matching and port isolation for all frequency bands of interest). On the other hand, because of well-defined shapes of the *S*-parameter responses for this class of components, feature-based optimization seems to be well suited to control multiple figures of interest as demonstrated in this work. Two-level EM modeling is used for further design cost reduction. More importantly, we develop a procedure for automated determination of the low-fidelity EM model coarseness that allows us to find the fastest possible model that still ensures sufficient correlation with its high-fidelity counterpart, which is critical for robustness of the optimization process. Our approach is illustrated using two dual-band compact couplers. Experimental validation is also provided.

Keywords: Dual-band couplers, multi-band couplers, compact microstrip structures, simulation-driven design, variable-fidelity simulations, feature-based optimization, model fidelity selection.

1. Introduction

Microstrip branch-line couplers (BLCs) are important microwave/RF components widely used in various systems such as Butler matrices [1], [2], circular polarization antennas [3], [4] or crossovers [5], [6]. Conventional coupler structures are four-port devices implemented using four quarter-wavelength transmission line sections. The typical performance specifications of BLCs are to provide equal power split and 90-degree phase shift between the transmission and the coupling ports at a given operating frequency [7]. Additionally, they should ensure sufficient matching and isolation at and around the operating frequency, which is enforced by simultaneously imposing requirements for −20 dB bandwidth for S_{11} and S_{41} [8]. For dual- and multi-band couplers, the aforementioned requirements are supposed to be fulfilled for several operating frequencies at the same time [9]-[11].

An important drawback of traditional BLCs—just as majority of other circuits constructed using conventional transmission lines—is their large footprint [12], [13]. There have been several methods developed over the years for reducing BLC sizes [8], [12]-[16]. Perhaps the most efficient strategies are those based on replacing the transmission lines of the conventional circuit with their corresponding slow-wave structures [13]. Other interesting techniques employ ground plane perforations [15], or modifications of the transmission lines by means of fractal geometries [16]. Utilization of unconventional topologies may result in over 85 percent miniaturization rate [15], [17]. However, size reduction is achieved at the expense of performance degradation. Typically, a reduced operational bandwidth is observed, as well as deviations from the ideal phase shift and/or equal power split. Consequently, the practical designs are normally trade-offs between the structure size and its electrical performance [8], [18].

Clearly, BLC design process becomes even more challenging (especially in terms of the size reduction) for multi-band couplers. In particular, the miniaturization techniques developed for single-band circuits cannot be adopted for multi-band structures in a straightforward way. This is mostly a consequence of low-pass properties of the transmission line modifications [15]. The compact dual-band BLC designs proposed in the literature (e.g., [19], [20]), are usually based on local alterations in the form of the circuit bends or stepped impedance resonators and they do not lead to considerable miniaturization rate. It seems that significant size reduction requires global BLC geometry modification, i.e., realized at the level of the entire circuit rather than locally, i.e., at the level of the individual transmission lines. Such modifications should be dedicated to the coupler structure at hand and formed to densely fill the interior of the BLC [15], [18], [19].

Selecting an appropriate miniaturization method and development of a coupler topology is just one of the necessary steps of design process. Another, just as important step, is adjustment of the structure dimensions. It is challenging because of the necessity of fulfilling many requirements concerning matching, power split, port isolation, bandwidth, etc., independently for each operating frequency. As mentioned earlier, compact designs introduce multiple cross-couplings within the structure. Some important consequences affecting the design process are [8], [17]: (i) equivalent circuit models are not reliable, (ii) accurate evaluation requires full-wave EM analysis, (iii) parameter-sweep-based procedures are inefficient and prone to failure. A recommended approach is automated design through simultaneous numerical optimization of all relevant geometry parameters. However, conventional optimization algorithms may be impractical due to excessive computational cost [21]. Design speedup can be obtained using surrogate-based optimization (SBO) [21]-[24]. One of the most popular SBO methods in microwave engineering is space mapping (SM) [21], [24]. Unfortunately, its application to compact circuit design is limited because of poor generalization of the surrogate model constructed from equivalent network representations [21].

Recently, feature-based optimization techniques have been introduced for handling expensive EM-driven design problems [25], [26], where close-to-linear dependence of the suitably defined characteristic points of the response on geometry parameters results in considerable cost reduction compared to directly optimizing the original responses of the structure (*S*-parameters versus frequency). In [11], feature-based optimization has been successfully demonstrated for a dual-band BLC. Here, we extend the work of [11] in two different ways: (i) we implement feature-based BLC design in a variable-fidelity EM simulation setting, and (ii) develop a procedure for automated selection of low-fidelity EM model discretization level. While (i) leads to further design cost reduction compared to [11], (ii) results in the best possible speedup while ensuring robustness. Numerical examples illustrate the benefits of variable-fidelity feature-based design and the importance of appropriate model coarseness adjustment. Experimental validation is also provided.

2. Feature-Based Optimization of Compact Couplers with Automated Model Fidelity Selection

In this section, a variable-fidelity feature-based optimization scheme for compact multi-band BLC design is formulated. Its important part is an automated procedure for model coarseness

adjustment. It is based on correlation analysis of the feature spaces of EM models of various fidelities and allows us to select the fastest possible simulation setup that still ensures design robustness.

2.1. Response Features for Multi-Band Couplers

In the design of coupler structures, the design objectives are normally formulated in terms of the scattering parameters and include (i) achieving equal power split (i.e., $|S_{21}| = |S_{31}|$) as well as (ii) minimization of $|S_{11}|$ and $|S_{41}|$. Both objectives are to be simultaneously fulfilled for one (for single-band couplers) or several operating frequencies (for multi-band couplers), denoted here as f_k, $k = 1, \ldots, N_f$, The second objective is often formulated in terms of obtaining sufficient −20 dB bandwidth for both $|S_{11}|$ and $|S_{41}|$.

The typical responses for a compact dual-band coupler are shown in Fig. 1. These are the actual characteristics of the structure considered in Section 3. One can notice that the responses are highly nonlinear as functions of frequency, therefore, difficult to optimize. Here, we utilize the concept of response features and feature-based optimization [25] to accelerate the optimization process. Because we are interested in ensuring equal power split as well as good matching and isolation at all operating frequencies f_k, the features of interest are selected as local maxima of $|S_{21}|$ and $|S_{31}|$ and minima of $|S_{11}|$ and $|S_{41}|$ around f_1 and f_2. Some of these points are marked in Fig. 1. Each feature point is characterized by the two coordinates: frequency (F) and level (L). Figure 2 shows a family of coupler responses of Fig. 1 corresponding to designs along certain line segment in the design space. Note that despite of highly nonlinear dependence of S-parameters on the coupler geometry, behavior of the feature points (cf. Fig. 3) is close to linear. Consequently, expressing the design goals in terms of the feature points and using feature-based surrogates is expected to speed up the optimization process considerably.

2.2. Design Problem Formulation in Feature Space

The coupler design problem is formulated in the feature space as [25]:

$$\boldsymbol{x}^* = \arg\min_{\boldsymbol{x}} U(\boldsymbol{F}(\boldsymbol{x}), \boldsymbol{L}(\boldsymbol{x})) \tag{1}$$

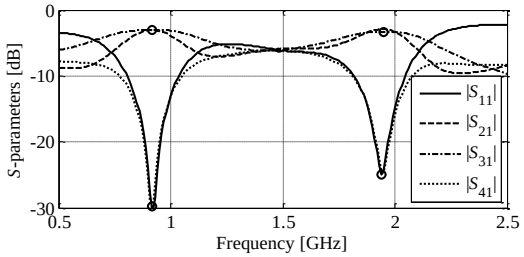

Fig. 1. Typical responses of a dual-band coupler [11]. Selected feature points are marked with the circles (here, corresponding to the maximum of $|S_{21}|$ around the lower operating frequency f_1, maximum of $|S_{31}|$ around the higher operating frequency f_2, as well as the two minima: of $|S_{41}|$ around f_1, and of $|S_{11}|$ around f_2).

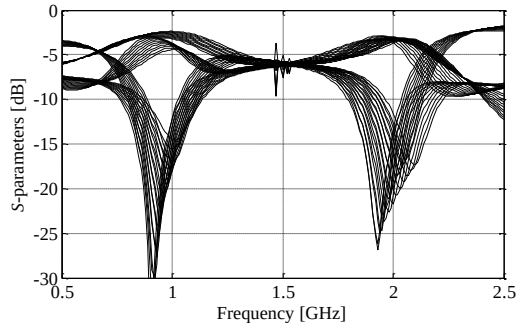

Fig. 2. Family of coupler responses corresponding to its geometries along certain line segment in the design space showing highly nonlinear behavior of *S*-parameters on geometry variables of the circuit.

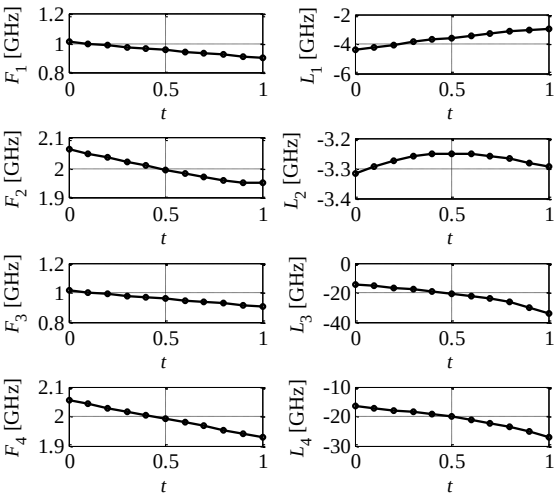

Fig. 3. Selected feature points (as marked in Fig. 1) corresponding to coupler geometries along the same line segment parameterized by t as in Fig. 2. Note that dependence of feature coordinates on coupler geometry is close to linear.

where U is the objective function formulated in terms of the feature vectors $\boldsymbol{F}(\boldsymbol{x})$ and $\boldsymbol{L}(\boldsymbol{x})$ (i.e., frequency and level coordinates of the respective feature points). The objective , where $\boldsymbol{x}$ is a vector of geometry parameters to be adjusted. The objective function is defined as the maximum of the feature point levels corresponding to the minima of $|S_{11}|$ and $|S_{41}|$ at all operating frequencies with

added penalty terms that are proportional to the deviations between the frequency coordinates of all feature points and the respective operating frequencies. Thus, the primary objective is to improve matching and isolation at all the operating frequencies f_k, $k = 1, \ldots, N_f$, and move the points of equal power split as close to the respective frequencies f_k as possible. The objective function is given as

$$U(\boldsymbol{F}(\boldsymbol{x}), \boldsymbol{L}(\boldsymbol{x})) = \max_{k=1,\ldots,N_f} \{l_{11.k}, l_{41.k}\} + \beta_1 \sum_{k=1}^{N_f} (f_{11.k} - f_{0.k})^2 + \beta_2 \sum_{k=1}^{N_f} (f_{41.k} - f_{0.k})^2 \tag{2}$$

where $l_{11.k}$ and $l_{41.k}$ are feature point level coordinates of the feature points corresponding to matching and isolation minima, whereas $f_{11.k}$ and $f_{41.k}$ are frequency coordinates of the same points; $f_{0.k}$ are required operating frequencies of the coupler. We also consider the following equality constraints:

$$c_k(\boldsymbol{L}(\boldsymbol{x})) = 0, \quad k = 1, \ldots, N_f \tag{3}$$

which are formulated in terms of the feature point level coordinates, i.e., $c_k = l_{21.k} - l_{31.k}$, where $l_{21.k}$ and $l_{31.k}$ are the feature point levels corresponding to the maxima of $|S_{21}|$ and $|S_{31}|$ around the operating frequency f_k. The constraints (3) allow for enforcing equal power split at all frequencies. In practice, they are also handled through penalty terms similar to those utilized in the objective function.

2.3. Variable-Fidelity Feature-Based Optimization Algorithm

The feature points can be extracted from the known *S*-parameter response of the coupler. However, direct solving of the problem (1) would still be expensive when executed using conventional methods (although cheaper than minimizing objectives formulated in terms of the *S*-parameters vs. frequency). Instead, we carry out the following iterative procedure

$$\boldsymbol{x}^{(i+1)} = \arg \min_{\|\boldsymbol{x} - \boldsymbol{x}^{(i)}\| \le r^{(i)}} U(\boldsymbol{F}_S^{(i)}(\boldsymbol{x}), \boldsymbol{L}_S^{(i)}(\boldsymbol{x})) \tag{4}$$

with the constraints

$$c_k^{(i)}(\boldsymbol{L}_S^{(i)}(\boldsymbol{x})) = 0, \quad k = 1, \ldots, N_f \tag{5}$$

In the above formulation, the sequence $\boldsymbol{x}^{(i)}$, $i = 0, 1, \ldots$, approximates the solution $\boldsymbol{x}^*$ to the original problem (1). The functions $\boldsymbol{F}_S^{(i)}$ and $\boldsymbol{L}_S^{(i)}$ are linear approximation models of the feature point vectors $\boldsymbol{F}(\boldsymbol{x})$ and $\boldsymbol{L}(\boldsymbol{x})$ established at the current design $\boldsymbol{x}^{(i)}$ using *n* perturbed designs around $\boldsymbol{x}^{(i)}$ and the corresponding feature points. In order to further reduce the design cost, the perturbed designs are obtained at the level of the low-fidelity EM simulation model, denoted as $\boldsymbol{F}_c(\boldsymbol{x})$ and $\boldsymbol{L}_c(\boldsymbol{x})$ for the feature point frequencies and levels, respectively. More specifically, we have

$$\boldsymbol{F}_S^{(i)}(\boldsymbol{x}) = \boldsymbol{F}(\boldsymbol{x}^{(i)}) + \left[\frac{\boldsymbol{F}_c(\boldsymbol{x}^{(i)} + \boldsymbol{h}_1) - \boldsymbol{F}_c(\boldsymbol{x}^{(i)})}{h} \quad \ldots \quad \frac{\boldsymbol{F}_c(\boldsymbol{x}^{(i)} + \boldsymbol{h}_n) - \boldsymbol{F}_c(\boldsymbol{x}^{(i)})}{h} \right]^T \cdot (\boldsymbol{x} - \boldsymbol{x}^{(i)}) \tag{6}$$

and

$$\boldsymbol{L}_S^{(i)}(\boldsymbol{x}) = \boldsymbol{L}(\boldsymbol{x}^{(i)}) + \left[\frac{\boldsymbol{L}_c(\boldsymbol{x}^{(i)} + \boldsymbol{h}_1) - \boldsymbol{L}_c(\boldsymbol{x}^{(i)})}{h} \quad \ldots \quad \frac{\boldsymbol{L}_c(\boldsymbol{x}^{(i)} + \boldsymbol{h}_n) - \boldsymbol{L}_c(\boldsymbol{x}^{(i)})}{h} \right]^T \cdot (\boldsymbol{x} - \boldsymbol{x}^{(i)}) \tag{7}$$

where $\boldsymbol{h}_k = [0 \ \ldots \ 0 \ h \ 0 \ \ldots \ 0]^T$ with h at kth position is obtained based on sensitivity analysis. Thus, construction of the models $\boldsymbol{F}_S^{(i)}$ and $\boldsymbol{L}_S^{(i)}$ requires a single EM simulation of the coupler structure at the high-fidelity (original model) level, and n evaluations of the low-fidelity EM model (here, n is the number of designable parameters). Note that because of the model definition the surrogate (6), (7) agrees exactly with $\boldsymbol{F}(\boldsymbol{x})$ and $\boldsymbol{L}(\boldsymbol{x})$ at the current design $\boldsymbol{x}^{(i)}$, i.e., $\boldsymbol{F}(\boldsymbol{x}^{(i)}) = \boldsymbol{F}_s^{(i)}(\boldsymbol{x}^{(i)})$ and $\boldsymbol{L}(\boldsymbol{x}^{(i)}) = \boldsymbol{L}_s^{(i)}(\boldsymbol{x}^{(i)})$.

As mentioned before, due to only slightly nonlinear dependence of the feature points on $\boldsymbol{x}$, generalization capability of the linear expansion models (6) and (7) will be very good so that the number of iterations (4) (thus, the overall optimization cost) is expected to be low. It is also worth noticing that the constraint functions (5) are approximated through the linear expansion model for $\boldsymbol{L}(\boldsymbol{x})$, however, upon convergence of the optimization process, they converge to the "true" constraints by definition of $\boldsymbol{L}_S^{(i)}$.

The algorithm (4) is embedded in trust-region framework [27] with the search radius $r^{(i)}$ updated using the standard rules [27].

2.4. Automated Low-Fidelity Model Selection through Correlation Analysis

Because of using the low-fidelity model for computing the linear part of the surrogates (6) and (7), it is critically important that the low-fidelity models $\boldsymbol{F}_c$ and $\boldsymbol{L}_c$ are sufficiently well correlated with the high-fidelity model $\boldsymbol{F}$ and $\boldsymbol{L}$. Because the low-fidelity model is only present in (6) and (7) through its estimated sensitivity, the absolute alignment between the low- and high-fidelity models is not of concern. The emphasis is put on sufficiently good alignment of the feature point gradients with respect to the designable parameters, both for the frequency and the level components. In this section, we develop a simple yet automated procedure for determining an appropriate discretization level for the low-fidelity model.

Let $\boldsymbol{x}_a$ be an arbitrary design (e.g., an initial design) and $\boldsymbol{x}_b$ be its perturbation (in arbitrary direction but small). Normally, perturbation size of up to three percent of the design space size is sufficient, however exact values have to be determined based on sensitivity analysis. We define the following vectors:

$$\Delta \boldsymbol{F} = \boldsymbol{F}(\boldsymbol{x}_b) - \boldsymbol{F}(\boldsymbol{x}_a), \qquad \Delta \boldsymbol{L} = \boldsymbol{L}(\boldsymbol{x}_b) - \boldsymbol{L}(\boldsymbol{x}_a) \tag{8}$$

$$\Delta \boldsymbol{F}_c = \boldsymbol{F}_c(\boldsymbol{x}_b) - \boldsymbol{F}_c(\boldsymbol{x}_a), \qquad \Delta \boldsymbol{L}_c = \boldsymbol{L}_c(\boldsymbol{x}_b) - \boldsymbol{L}_c(\boldsymbol{x}_a) \tag{9}$$

which describe the changes of the feature points (frequency and level components) for the high-model and the low-fidelity model, respectively. Subsequently, the linear regression of the data sets $\{\Delta \boldsymbol{F}, \Delta \boldsymbol{F}_c\}$ and $\{\Delta \boldsymbol{L}, \Delta \boldsymbol{L}_c\}$ is calculated, and the coefficient of determination r^2 [28] is computed for both sets. The coefficient r^2 describes how well the low- and high-fidelity data sets are correlated, in other words, what is the confidence level when using the low-fidelity model (instead the high-fidelity one) for sensitivity estimation in (6) and (7). Perfect correlation corresponds to $r^2 = 1.0$. Here, we take $r^2 = 0.9$ as sufficient correlation level.

In practice, a family of low-fidelity models with various (increasing) discretization levels is considered. In this work, we utilize CST Microwave Studio [29] for EM analysis, and the LPW parameter (lines per wavelength) is selected for setting up the discretization level of the model. The high-fidelity model corresponds to LPW = 40. We use LPW = 8 and up for the low-fidelity models.

Figure 4 shows the scatter plots $\Delta \boldsymbol{F}_c$ versus $\Delta \boldsymbol{F}$ and $\Delta \boldsymbol{L}_c$ versus $\Delta \boldsymbol{L}$, along with the regression lines, for the coupler of Section 3 for the three values of LPW: 10, 16, and 26. It can be observed that the model with LPW = 10 is clearly too coarse, especially in terms of the level components. Alignment is greatly improved for LPW = 16; however, the deviations from the regression line seem still too large for the level components. The model with LPW = 26 exhibits very good correlations with the high-fidelity model.

Figure 5 shows the r^2 plots for the range of LPW values from 8 to 40. The value of r^2 is very low for LPW smaller than 15 and stabilizes for LPW > 20. Obviously, $r^2 = 1$ for LPW = 40. It can also be seen that—especially for higher values of LPW—correlation is better for the level components than for the frequency components. An important aspect is that the values of r^2 exhibit large fluctuations, particularly for small values of LPW. This is partially the effect of the numerical noise (decreasing with the increase of the discretization density) but also an arbitrary choice of the reference design. Therefore, for the sake of the model selection, we calculate the

moving average of the r^2 values (calculated for the three consecutive points along the characteristic) and then consider the mean of the frequency and the level characteristics. As indicated in Fig. 5, the mean is much smoother than the "raw" characteristics. For the acceptance level for r^2 equal to 0.9, the threshold value of LPW = 22.

Based on the considerations above, the procedure for low-fidelity model selection can be summarized as follows:

- Evaluate the EM model at two designs $\boldsymbol{x}_a$ and $\boldsymbol{x}_b$ as described above for the preselected range of LPW;
- Obtain the mean of the correlation parameters characteristics r^2 for the data sets $\{\Delta\boldsymbol{F}, \Delta\boldsymbol{F}_c\}$ and $\{\Delta\boldsymbol{L}, \Delta\boldsymbol{L}_c\}$ for all LPW values;
- Select the low-fidelity model for which the mean r^2 is larger than 0.9.

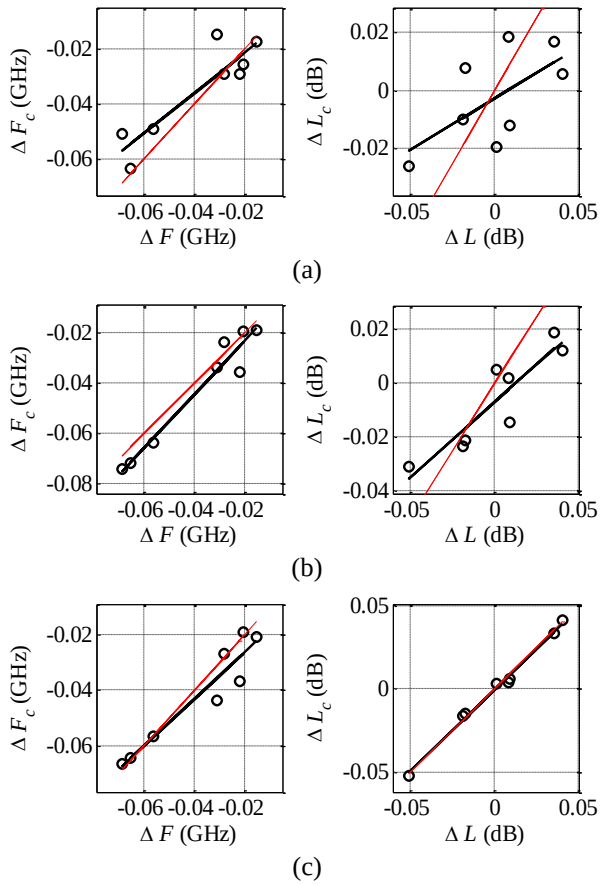

Fig. 4. Scatter plots $\Delta\boldsymbol{F}_c$ versus $\Delta\boldsymbol{F}$ (left) and $\Delta\boldsymbol{L}_c$ versus $\Delta\boldsymbol{L}$ (right) for the three low-fidelity models defined with LPW = 10 (a), 16 (b), and 26 (c). The black solid lines denote the linear regression function; the red lines are regression functions for the reference data sets $\{\Delta\boldsymbol{F}, \Delta\boldsymbol{F}\}$ and $\{\Delta\boldsymbol{L}, \Delta\boldsymbol{L}\}$.

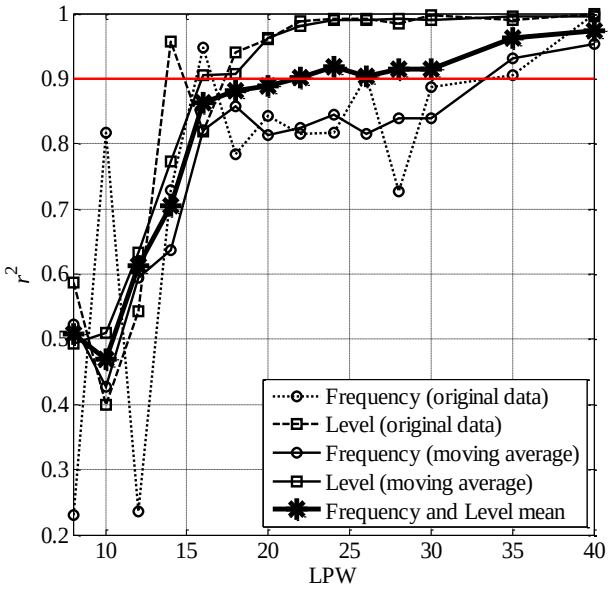

Fig. 5. r^2 plots for the $\{\Delta\boldsymbol{F}, \Delta\boldsymbol{F}_c\}$ and $\{\Delta\boldsymbol{L}, \Delta\boldsymbol{L}_c\}$ data sets versus model discretization level (here, determined by the LPW parameter). Original data plotted using dotted (frequency components) and dashed lines (level component). Moving averages plotted with continuous line, whereas the frequency/level mean plotted using thick line with star markers. Acceptable confidence level (0.9) is marked using a horizontal line.

It should be noted that the procedure is computationally cheap because coarse-discretization EM simulations are considerably faster than the high-fidelity ones (the overall cost corresponds to just a few evaluations of the high-fidelity EM model). The procedure is fully automated. The examples discussed in Section 3 and 4 indicate the importance of an appropriate low-fidelity model setup both from the point of view of the reliability of the optimization process and its computational cost.

3. Design Case I: Compact Dual-Band BLC I

In this section, we discuss a compact dual-band branch-line coupler structure designed for the two operating frequencies f_1 = 0.92 GHz and f_2 = 1.9 GHz. Description of the coupler structure is followed by the numerical results and comparison with the benchmark methods, including single-fidelity feature-based optimization. Experimental validation is also provided.

3.1. Coupler Structure

Consider a compact dual-band branch-line coupler shown in Fig. 6 [11]. The circuit is implemented on Taconic RF-35 dielectric substrate (h = 0.762 mm; ε_r = 3.5; tanδ = 0.0018). The

structure is constructed using the transmission lines of three different characteristic impedances with equal electrical lengths [9]. The compact design is based on conventional dual-band BLC realization and modified so that the interior of a coupler is filled as much as possible. The BLC geometry is described by seven independent adjustable parameters $\boldsymbol{x} = [w_1\ w_2\ w_3\ l_1\ l_2\ l_3\ l_{31}]^T$. The dependent variables are $l_{1m} = 0.2 \cdot |l_3 + 3w_3 + 3l_{3m} - 4w_1|$, $l_{2m} = 0.2 \cdot (l_3 + w_3 + l_{3m} + 0.5w_1 - 4.5w_2)$ and $l_{32} = w_1 + l_1 - w_3$, whereas $l_{3m} = 0.2$ and $w_0 = 1.7$ (the unit is mm). The area occupied by the coupler is defined as $A \times B$ rectangle with $A = 2 \cdot (l_1 + 2w_1) + 5w_3 + 6l_{3m}$ and $B = 2 \cdot (5w_1 + 5l_{1m}) + w_3$. The high-fidelity EM model of the structure is implemented in CST Microwave Studio (~500,000 mesh cells; LPW = 40). Its average simulation time is 15 min.

The following design objectives are considered in the optimization process: (i) equal power split between the transmission and the coupling ports (i.e., $|S_{21}| = |S_{31}|$), (ii) minimization of the return loss $|S_{11}|$, and (iii) minimization of isolation $|S_{41}|$. The assumed operating frequencies are $f_1 = 0.92$ GHz and $f_2 = 1.9$ GHz. The physical consistency of the circuit geometry is ensured by imposing the following lower and upper bounds for design variables: $\boldsymbol{l} = [0.7\ 0.3\ 0.5\ 6\ 6\ 4\ 10]^T$ and $\boldsymbol{u} = [1.7\ 1.3\ 1.5\ 10\ 10\ 8\ 14]^T$.

The low-fidelity model has been selected by considering various values of LPW in the range from 8 to 40. The selected scatter plots as well as the r^2 plots have been presented in Figs. 4 and 5, respectively. Based on this analysis, the model with LPW = 22 has been selected as the low-fidelity model for the variable-fidelity feature-based optimization as described in Section 2.

3.2. Numerical Results. Low-Fidelity Model Selection Impact

The initial design $\boldsymbol{x}^{(0)} = [1.39\ 0.58\ 0.99\ 8.66\ 9.19\ 5.02\ 12.73]^T$ mm has been obtained by optimizing the equivalent circuit model of the circuit. Figure 7 shows the responses at $\boldsymbol{x}^{(0)}$ indicating non-equal power split at both operating frequencies as well as the frequency shift for matching and isolation characteristics for f_2.

The final design $\boldsymbol{x}^* = [1.45\ 0.55\ 0.87\ 9.01\ 9.82\ 5.16\ 12.04]^T$ mm has been obtained after three iterations of the algorithm (4), (5). The footprint of the coupler is $29.3 \times 34.2 = 1002$ mm^2. The circuit responses are shown in Fig. 8. It can be observed that they are well centred around the operating frequencies, and almost equal power split has been achieved ($|S_{21}| - |S_{31}| < 0.03$ dB for f_1, and $|S_{21}| - |S_{31}| < 0.1$ dB for f_2).

For the sake of comparison, direct optimization (from $\boldsymbol{x}^{(0)}$) of the coupler structure at the level

of *S*-parameters vs. frequency has been conducted using a pattern search algorithm (setup: minimum grid size 0.01 mm, grid reduction factor 3, perturbations obtained based on sensitivity analysis) [30]. A design of a similar quality has been obtained, however, at a much higher computational cost of 122 evaluations of the EM coupler model.

The importance of the low-fidelity model selection has been illustrated by executing a single-fidelity feature-based optimization (or, equivalently, the low-fidelity model of LPW = 40, i.e., identical to the high-fidelity one), as well as variable-fidelity optimization with the low-fidelity model of LPW = 10 (i.e., too coarse according to the correlation analysis of Section 2.4. In the first case, a similar final design was obtained, however, at a much higher computational cost. In the second case, the algorithm started diverging already after the first iteration (cf. Fig. 9), indicating that the low-fidelity model with LPW = 10 does not provide reliable estimation of the feature point gradients.

The cost breakdown for all considered optimization approaches has been gathered in Table 1.

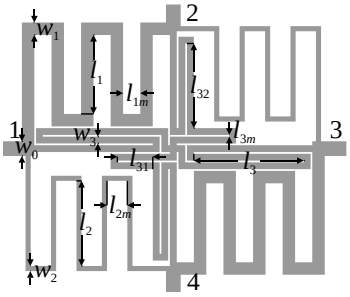

Fig. 6. Geometry of a compact dual-band branch-line coupler (BLC I).

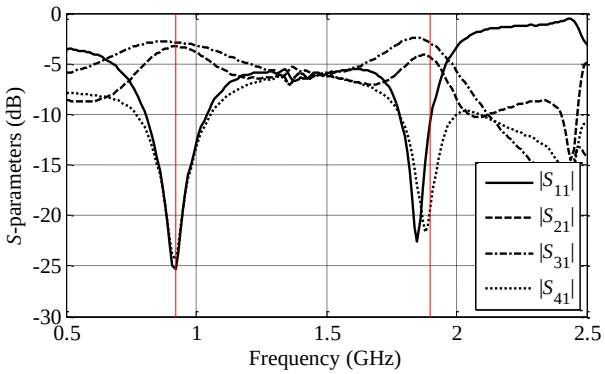

Fig. 7. Responses of the compact dual-band coupler at the initial design. Operating frequencies f_1 = 0.92 GHz and f_2 = 1.90 GHz are marked using vertical lines.

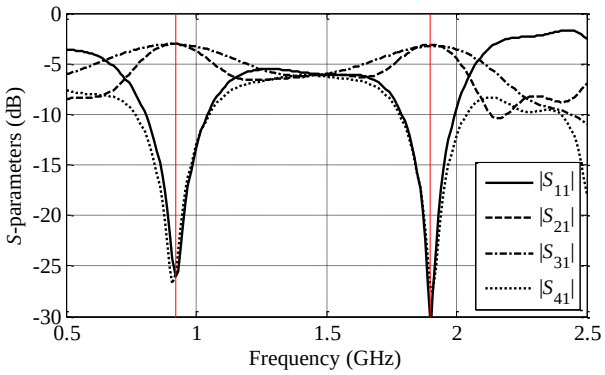

Fig. 8. Responses of the compact dual-band coupler at the design obtained by feature-based optimization using the low-fidelity model with LPW = 22. Operating frequencies f_1 = 0.92 GHz and f_2 = 1.90 GHz are marked using vertical lines.

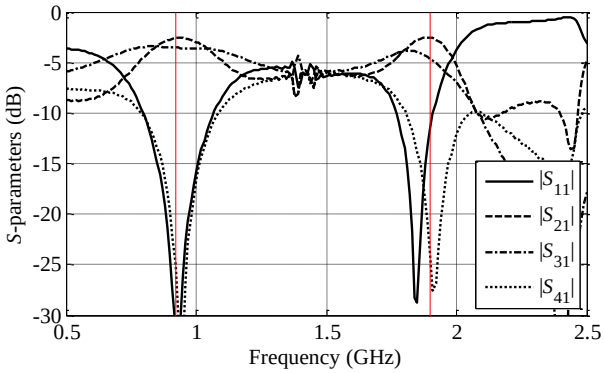

Fig. 9. Responses of the dual-band coupler after first iteration of the feature-based optimization using the low-fidelity model with LPW = 10. Divergence towards a poor design can be observed indicating that the low-fidelity model is too coarse to provide reliable estimation of the feature point gradients.

Table 1: Dual-Band Coupler I Optimization. Design Cost

Algorithm	Number of Model Evaluations		Optimization Cost	
	Low-Fidelity	High-Fidelity	Absolute [hours]	Relative to High-Fidelity Model
Variable-Fidelity Feature-Based (Low-Fidelity Model with LPW = 22)	24	4	2.3	9.3
Single-Fidelity Feature-Based (Low-Fidelity Model with LPW = 40)	-	25	6.25	25.0
Variable-Fidelity Feature-Based (Low-Fidelity Model with LPW = 10)	N/A (algorithm divergent)			
Pattern Search [30]	-	122	30.5	122.0

3.3. Experimental Validation and Comparisons

The optimized coupler structure has been fabricated and measured. A photograph of the manufactured circuit is given in Fig. 10, whereas Fig. 11 shows comparison of the simulated and measured characteristics. The agreement between the results is acceptable. Small frequency shift for the upper operating frequency is due to using simplified EM model of the structure that lack SMA connectors.

Performance characteristics of the coupler are gathered in Table 2. It should be noted that the power split level is slightly lower for the measured coupler responses, which is due to higher losses introduced by the connectors, as well as tolerance of the fabrication process. On the other hand, the power split imbalance is similar to the simulated results. For the measured structure, the bandwidth BW_1, defined as the frequency range where both return loss $|S_{11}|$ and isolation $|S_{41}|$ are below –20 dB level, is 6.5% and 3.5% for f_1 and f_2, respectively. The bandwidth BW_2 (defined as $||S_{21}| - |S_{31}|| \leq 0.2$ dB) is 12% for 0.92 GHz and 3% for 1.9 GHz.

4. Design Case II: Compact Dual-Band BLC II

Here, we present the second example, which is also a compact dual-band branch-line coupler, designed for the two operating frequencies f_1 = 0.9 GHz and f_2 = 2.0 GHz. Numerical results are accompanied by experimental validation of the fabricated coupler prototype.

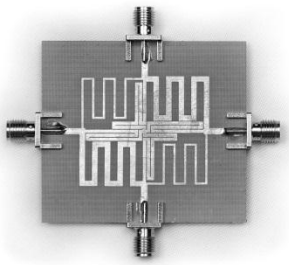

Fig. 10. Photograph of the fabricated prototype of the dual-band branch-line coupler of Fig. 6 (Coupler I).

Table 2: Simulated vs. Measured BLC I Responses

	Simulation		Measurement	
	f_1	f_2	f_1	f_2
S_{11} [dB]	–26.1	–31.1	–38.0	–37.1
S_{21} [dB]	–3.03	–3.08	–3.24	–3.42
S_{31} [dB]	–3.07	–3.23	–3.34	–3.76
S_{41} [dB]	–25.8	–27.0	–25.2	–24.5
BW_1 [GHz]	0.89 to 0.94	1.88 to 1.93	0.87 to 0.93	1.84 to 1.91
BW_2 [GHz]	0.86 to 0.97	1.83 to 1.96	0.84 to 0.95	1.89 to 1.95

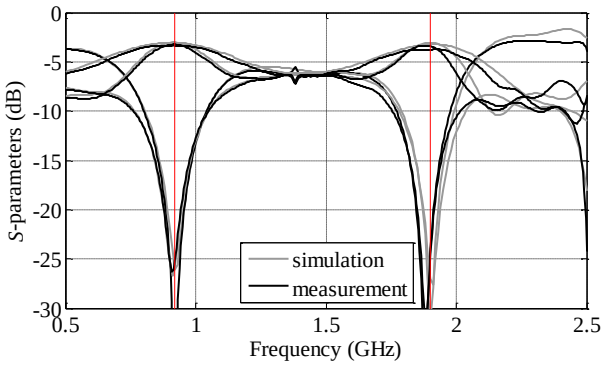

Fig. 11. The measured (black line) and simulated (gray dashed line) scattering parameters of the compact dual-band branch-line coupler (BLC I). The simulation has been performed using LPW = 40.

4.1. Coupler Structure

Consider a novel compact dual-band branch-line coupler shown in Fig. 12. The circuit is implemented on Taconic RF-35 dielectric substrate (h = 0.762 mm; ε_r = 3.5; tanδ = 0.0018). The structure is constructed using three types of transmission lines. The miniaturized design is based on conventional realization of a dual-band branch-line coupler with quarter-wave open circuit stubs [10]. The introduced geometry modifications include folding sections and meandering of the stubs, both to the interior of the circuit. The structure is described by a vector of nine adjustable parameters: $\boldsymbol{x} = [l_1\ l_2\ l_3\ s_1\ s_2\ s_3\ w_1\ w_2\ w_3]^T$. The dependent parameters are $l_{11} = 4w_3 + 4s_3 + s_1$, $l_{21} = \max\{l_3 + s_3 + s_2 + 2w_3, w_1 + l_1\} + s_2$, whereas w_0 = 1.7 mm to ensure 50 Ohm input impedance (all parameters are in mm). The coupler footprint is defined as $A \times B$ rectangle where $A = 2(l_{21} + w_2 + w_1) + s_2$ and $B = 2(w_2 + s_3 + w_3 + l_{11} + w_1) + s_1$. The high-fidelity EM model of the structure is implemented in CST Microwave Studio (~860,000 mesh cells; LPW = 40). Its average simulation time is 18 min.

The design objectives are the same as for the first examples: (i) equal power split between the transmission and the coupling ports (i.e., $|S_{21}| = |S_{31}|$), (ii) minimization of the return loss $|S_{11}|$, and (iii) minimization of isolation $|S_{41}|$. The assumed operating frequencies are f_1 = 0.9 GHz and f_2 = 2.0 GHz. The following lower and upper bounds are assumed for the design variables: $\boldsymbol{l}$ = [4.0 4.0 4.0 0.2 0.2 0.2 0.5 0.5 0.5]^T and $\boldsymbol{u}$ = [9.0 9.0 9.0 0.6 0.6 0.6 2.0 2.0 2.0]^T.

The low-fidelity model has been selected by considering various values of LPW in the range from 8 to 40. The r^2 plots are presented in Fig. 13. Based on this analysis, the model with LPW = 20 has been selected as the low-fidelity model for the variable-fidelity feature-based optimization as described in Section 2. Note that the condition $r^2 > 0.9$ is satisfied even for LPW = 16, however, a slightly higher value has been selected to ensure sufficient accuracy of the coupler model.

4.2. Numerical Results. Low-Fidelity Model Selection Impact

The initial design $\boldsymbol{x}^{(0)}$ = [8.71 4.00 8.00 0.60 0.47 0.20 1.60 0.92 0.97]^T mm has been obtained by optimizing the equivalent circuit model of the coupler. Figure 14 shows the responses at $\boldsymbol{x}^{(0)}$. It should be emphasized that the response is severely detuned with respect to the assumed design specifications. Also, this indicates poor agreement between the equivalent circuit model and the full-wave EM simulation one.

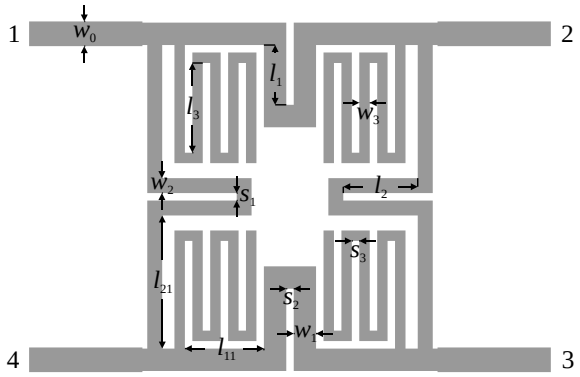

Fig. 12. Geometry of a compact dual-band branch-line coupler (Coupler II).

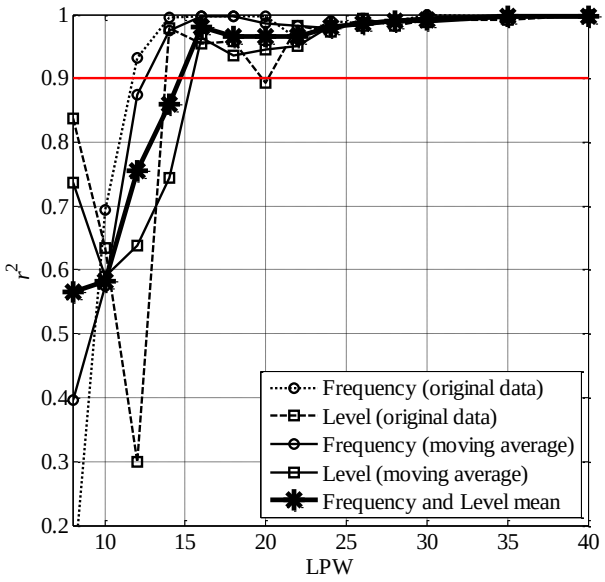

Fig. 13. r^2 plots for the {$\Delta\boldsymbol{F}$, $\Delta\boldsymbol{F}_c$} and {$\Delta\boldsymbol{L}$, $\Delta\boldsymbol{L}_c$} data sets versus model discretization level (here, determined by the LPW parameter) for Coupler II. Original data plotted using dotted (frequency components) and dashed lines (level component). Moving averages plotted with continuous line, whereas the frequency/level mean plotted using thick line with star markers. Acceptable confidence level (0.9) is marked using a horizontal line.

The final design $\boldsymbol{x}^* = [4.42\ 6.35\ 5.51\ 0.20\ 0.60\ 0.21\ 1.67\ 1.14\ 1.69]^T$ mm has been obtained after seven iterations of the algorithm (4), (5). The footprint of the coupler is 25.8 × 26.9 = 694 mm^2. The circuit responses are shown in Fig. 15. They are perfectly centred at the operating frequencies. Furthermore, nearly perfectly equal power split has been obtained ($|S_{21}| - |S_{31}| <$ 0.025 dB for f_1, and $|S_{21}| - |S_{31}| < 0.12$ dB for f_2).

Direct optimization of the coupler structure at the level of *S*-parameters vs. frequency has been conducted using a pattern search algorithm [30] yields a slightly worse design at a much higher cost of 160 evaluations of the EM coupler model.

Similarly as for the previous example, feature-based optimization was also conducted for the low-fidelity model set to LPW = 40 (i.e., single-fidelity optimization), and for LPW = 10. In the first case, the final design was obtained at six iterations of the algorithm (the cost of 55 high-fidelity model evaluations). In the second case, the algorithm was convergent due to limited accuracy of the low-fidelity model. The cost breakdown for all considered optimization approaches has been gathered in Table 3.

4.3. Experimental Validation and Comparisons

The optimized BLC II has been fabricated and measured. A photograph of the manufactured circuit and comparison of the simulated and the measured responses are provided in Figs. 16 and 17, respectively. Detailed data concerning coupler is provided in Table 4. The obtained simulation and measurement results are in good agreement, however a slight frequency shift for the upper operating frequency can be observed. Moreover, the power split level for the measured structure is slightly lower than for the EM model responses. Nonetheless, the results obtained by means of simulation exhibit similar power split imbalance. The discrepancies between simulations and measurements result from inaccuracy of the fabrication process, as well as from utilization of the EM model which lacks connectors. The measurements indicate that the bandwidth BW_1 where $|S_{11}|$ and $|S_{41}|$ are both below –20 dB level is 4.5% and 1.5% for 0.9 GHz and 2 GHz, respectively. At the same time, the bandwidth BW_2 (defined as $| |S_{21}| - |S_{31}| | \leq 0.2$ dB) is 10% for f_1 frequency and 2% for f_2 frequency.

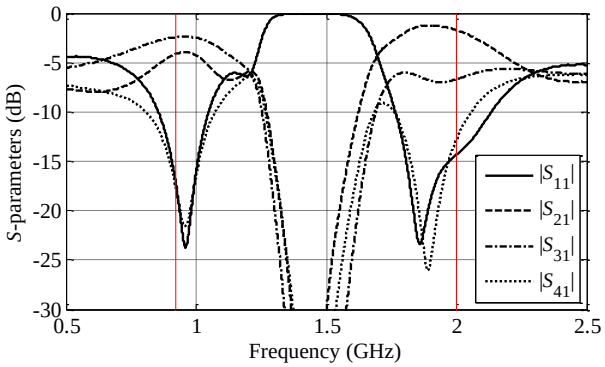

Fig. 14. Responses of the compact dual-band coupler (BLC II) at the initial design. Operating frequencies f_1 = 0.9 GHz and f_2 = 2.0 GHz are marked using vertical lines.

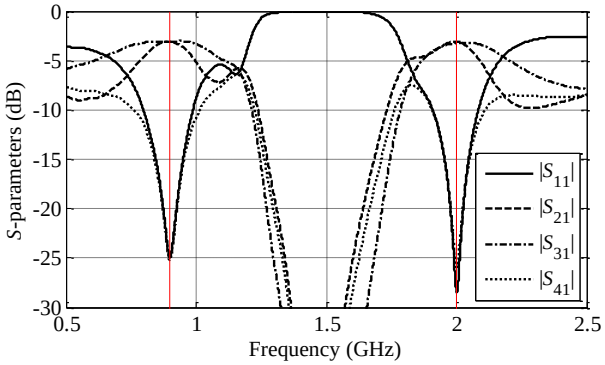

Fig. 15. Responses of the compact dual-band coupler (BLC II) at the design obtained by feature-based optimization using the low-fidelity model with LPW = 20. Operating frequencies f_1 = 0.9 GHz and f_2 = 2.0 GHz are marked using vertical lines.

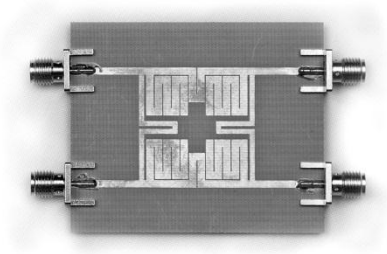

Fig. 16. Photograph of the fabricated prototype of the dual-band branch-line coupler of Fig. 12 (BLC II).

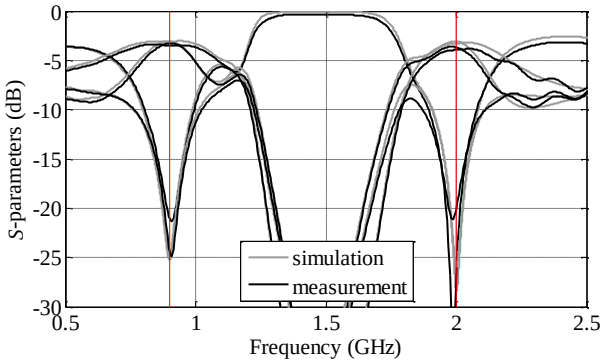

Fig. 17. The measured (black line) and simulated (grey dashed line) scattering parameters of the compact dual-band branch-line coupler (BLC II). The simulation has been performed using LPW = 40.

Table 3: Dual-band coupler ii optimization. Design cost

Algorithm	Number of Model Evaluations		Optimization Cost	
	Low-Fidelity	High-Fidelity	Absolute [hours]	Relative to High-Fidelity Model
Variable-Fidelity Feature-Based (Low-Fidelity Model with LPW = 20)	63	8	5.2	17.3
Single-Fidelity Feature-Based (Low-Fidelity Model with LPW = 40)	-	55	16.5	55.0
Variable-Fidelity Feature-Based (Low-Fidelity Model with LPW = 10)	N/A (algorithm divergent)			
Pattern Search [30]	-	160	48.0	160.0

Table 4: Simulated vs. Measured BLC II Responses

	Simulation		Measurement	
	f_1	f_2	f_1	f_2
S_{11} [dB]	–24.9	–28.4	–21.3	–27.4
S_{21} [dB]	–3.08	–3.08	–3.28	–3.67
S_{31} [dB]	–3.11	–3.27	–3.34	–3.76
S_{41} [dB]	–25.3	–25.9	–24.8	–21.1
BW_1 [GHz]	0.87 to 0.92	1.98 to 2.02	0.89 to 0.93	1.97 to 2.00
BW_2 [GHz]	0.86 to 0.93	1.87 to 2.04	0.86 to 0.95	2.00 to 2.04

5. Conclusion

Utilization of variable-fidelity feature-based optimization for rapid design closure of compact multi-band microstrip couplers has been demonstrated. We exploit surrogate-assisted optimization with the surrogate model constructed (of both objective function and constraints) from critical points—both frequency- and level-wise—of the highly nonlinear responses of the structure (i.e., S-parameters versus frequency). Design speedup has been achieved due to only slightly nonlinear dependence of the feature point coordinates on the geometry variables of the structures at hand. Further cost reduction has been obtained by using variable-fidelity EM models. An automated procedure for low-fidelity model setup has been proposed and implemented. As verified using the two case studies, it permits selecting the fastest low-fidelity model that still ensures robustness of the optimization process. Numerical results have been validated by physical measurements of the fabricated coupler prototypes.

Acknowledgement

The authors would like to thank Computer Simulation Technology AG, Darmstadt, Germany, for making CST Microwave Studio available. This work was supported in part by the Icelandic Centre for Research (RANNIS) Grant 130450051 and by National Science Centre of Poland Grant 2014/15/B/ST7/04683.

References

[1] C.-C. Chang, R.-H. Lee, T.-Y. Shih, "Design of a Beam Switching/Steering Butler Matrix for Phased Array System," *IEEE Trans. Ant. Prop.*, vol. 58, no. 2, pp. 367-374, 2010.

[2] C.-W. Wang, T.-G. Ma, and C.-F. Yang, "A New Planar Artificial Transmission Line and Its Applications to a Miniaturized Butler Matrix," *IEEE Trans. Microwave Theory Tech.*, vol. 55, no. 12, pp. 2792-2801, 2007.

[3] J.P. Thakur, J.-S. Park, "An advance design approach for circular polarization of the microstrip antenna with unbalance DGS feedlines," *IEEE Ant. Wireless Prop. Lett.*, vol. 5, no. 1, pp. 101-103, 2006.

[4] K. Kim, S. Lim, "Miniaturized Circular Polarized TE_{10}-Mode Substrate-Integrated-Waveguide Antenna," *IEEE Ant. Wireless Prop. Lett.*, vol. 13, pp. 658-661, 2014.

[5] F. Lin, Q.-X. Chu, S.W. Wong, "Dual-Band Planar Crossover With Two-Section Branch-Line Structure," *IEEE Trans. Microwave Theory Tech.*, vol. 61, no. 6, pp. 2309-2316, 2013.

[6] J.J. Yao, "Nonstandard Hybrid and Crossover Design With Branch-Line Structures," *IEEE Trans. Microwave Theory Tech.*, vol. 58, no. 12, pp. 3801-3808, 2010.

[7] D.M. Pozar, *Microwave Engineering*, 4th ed., John Wiley & Sons, 2012.

[8] A. Bekasiewicz, P. Kurgan, "A compact microstrip rat-race coupler constituted by nonuniform transmission lines," *Microwave Opt. Techn. Lett.*, vol. 56, no. 4, pp. 970-974, 2014.

[9] M.-J. Park, B. Lee, "Dual-band, cross coupled branch line coupler," *IEEE Microwave Wireless Comp. Lett.*, vol. 15, no. 10, pp. 655-657, 2005.

[10] K.-L.M. Cheng, F.-L. Wong, "A novel approach to the design and implementation of dual-band compact planar 90° branch-line coupler," *IEEE Trans. Microw. Theory Tech.*, vol. 52, no. 11, pp. 2458-2463, 2004.

[11] S. Koziel, and A. Bekasiewicz, "Efficient Design Optimization of Compact Dual-Band Microstrip Branch-Line Coupler Using Response Features," to appear, *IEEE MTT-S Int. Conf. Numerical EM Multiphysics Model. Opt. for RF, Microwave, THz App.*, Ottawa, 2015.

[12] S.-S. Liao, P.-T. Sun, N.-C. Chin, and J.-T. Peng, "A Novel Compact-Size Branch-Line Coupler," *IEEE Microw. Wireless Compon. Lett.*, vol. 15, no. 9, pp. 588–590, 2005.

[13] P. Kurgan, M. Kitlinski, "Novel doubly perforated broadband microstrip branch-line couplers," *Microwave Opt. Techn. Lett*., vol. 51, no. 9, pp. 2149-2152, 2009.

[14] C.-W. Tang, M.-G. Chen, "Synthesizing Microstrip Branch-Line Couplers With Predetermined Compact Size and Bandwidth," *IEEE Trans. Microwave Theory Tech.*, vol. 55, no. 9, pp. 1926–1934, Sept. 2007.

[15] P. Kurgan, J. Filipcewicz, M. Kitlinski, "Design considerations for compact microstrip resonant cells dedicated to efficient branch-line miniaturization," *Microwave Opt. Techn. Lett*., vol. 54, no. 8, pp. 1949-1954, 2012.

[16] P. Kurgan, M. Kitlinski, "Slow-wave fractal-shaped compact microstrip resonant cell," *Microwave Opt. Techn. Lett.*, vol. 52, no. 11, pp. 2613-2615, 2010.

[17] C.-H. Tseng, C,-L. Chang, "A Rigorous Design Methodology for Compact Planar Branch-Line and Rat-Race Couplers With Asymmetrical T-Structures," *Trans. Microw. Theory Tech.*, vol. 60, no. 7, pp. 2085-2092, 2012.

[18] K.-Y. Tsai, H.-S. Yang, J.-H. Chen, Y.-J.Chen, "A Miniaturized 3 dB Branch-Line Hybrid Coupler with Harmonics Suppression," *IEEE Microw. Wireless Comp. Lett.*, vol. 21, no. 10, pp. 537–539, Oct. 2011.

[19] K.-S. Chin, K.-M. Lin, Y.-H. Wei, T.-H. Tseng, Y.-J. Yang, "Compact Dual-Band Branch-Line and Rat-Race Couplers With Stepped-Impedance-Stub Lines," *Trans. Microw. Theory Tech.*, vol. 58, no. 5, pp. 1213-1221, 2010.

[20] M. Nosrati, M. Daneshmand, B.S. Virdee, "Novel compact dual-narrow/wideband branch-line couplers using T-Shaped stepped-impedance-stub lines," *Int. J. RF Microwave Comp. Aid. Eng.*, vol. 21, no. , pp. 642-649, 2011.

[21] A. Bekasiewicz, S. Koziel, B. Pankiewicz, "Accelerated Simulation-Driven Design Optimization of Compact Couplers by Means of Two-Level Space Mapping," *IET Microwaves, Antennas & Propagation*, vol. 9, no. 7, pp. 618-626, 2015.

[22] S. Koziel and X.S. Yang (Eds.), "Computational optimization, methods and algorithms," Series: Studies in Computational Intelligence, vol. 356, Springer, 2011.

[23] M.B. Yelten, T. Zhu, S. Koziel, P.D. Franzon, and M.B. Steer, "Demystifying surrogate modeling for circuits and systems," *IEEE Circuits and Systems Magazine*, vol. 12, no. 1, pp. 45-63, 2012.

[24] J.W. Bandler, Q.S. Cheng, S.A. Dakroury, A.S. Mohamed, M.H. Bakr, K. Madsen, J. Søndergaard, "Space mapping: the state of the art," *IEEE Trans. Microwave Theory Tech.*, vol. 52, no. 1, pp. 337-361, 2004.

[25] S. Koziel, J.W. Bandler, "Rapid Yield Estimation and Optimization of Microwave Structures Exploiting Feature-Based Statistical Analysis," *IEEE Trans. Microwave Theory Tech.*, vol. 63, no. 1, pp. 107-114, 2015.

[26] O. Glubokov, S. Koziel, "EM-driven tuning of substrate integrated waveguide filters exploiting feature-space surrogates," *IEEE MTT-S Int. Microwave Symp.*, pp. 1-3, 2014.

[27] A.R. Conn, N.I.M. Gould, and P.L. Toint, *Trust Region Methods*, MPS-SIAM Series on Optimization, 2000.

[28] N.R. Draper, H. Smith, *Applied regression analysis*, 3rd ed., Wiley Interscience, New York, 1998.

[29] CST Microwave Studio, ver. 2013, CST AG, Bad Nauheimer Str. 19, D-64289 Darmstadt, Germany, 2013.

[30] T.G. Kolda, R.M. Lewis, V. Torczon, "Optimization by direct search: new perspectives on some classical and modern methods," *SIAM Review*, vol. 45, no. 3, pp. 385-482, 2003.